# Numerical analysis of binary fluid convection with thermal and solutal lateral gradients

Juan Sánchez Umbría[*]

*Departament de Física, Universitat Politècnica de Catalunya.*

*Jordi Girona Salgado 1-3. Campus Nord. Mòdul B4. 08034 Barcelona. Spain*

Marta Net[†]

*Universitat Politècnica de Catalunya.*

*Barcelona. Spain*

(Dated: January 7, 2025)

## Abstract

This article analyzes the influence of laterally enforced solutal gradients on the steady and bifurcated periodic dynamics in binary fluids contained in horizontally heated slots, taking into account the Soret and Dufour effects. Numerical Newton-Krylov continuation techniques to follow the primary and secondary branches of steady solutions and periodic orbits are applied. The stability of all these branches is also analyzed. A great variety of stable steady and periodic states is found, depending on the ratio of the thermal and solutal gradients. The proximity to parameters that balance the buoyancy forces delays the onset of center-symmetric oscillations to very large values of the thermal Rayleigh number, while large solutal gradients tend to restabilize the steady flows after the onset of center-symmetric oscillations, and to give rise to spatio-temporal symmetric waves of broken center symmetry at larger thermal Rayleigh number. The work done by the thermal buoyancy force is essential for the restabilization of the steady states and the change of the ulterior dynamics. It is also shown that the transition to temporal chaos depends strongly on the absence or the intensity of the solutal gradients.

Keywords: Thermal convection, Binary mixtures, Steady and oscillatory flows, Stability

---

[*] juan.j.sanchez@upc.edu

[†] marta.net@upc.edu

## I.   INTRODUCTION

Thermosolutal and binary fluid convection has long been studied because of its relevance in natural phenomena concerning oceanography, astrophysics, geophysics, geology, etc., and in a large amount of industrial applications; among them crystal growth and metal manufacturing processes, storage of nuclear wastes, etc. Different features involving this problem have been analyzed for decades, however most of them without considering real gases with non-negligible Soret and Dufour interactions.

Convection problems involving large amounts of mass transfer are often studied theoretically and also numerically by considering permeable boundaries of constant concentration of the solute. The differential concentration generates vertical or horizontal gradients either in the direction of the thermal gradients or opposed to them, depending on the geometry of the problem. Some studies focus on the case in which the buoyancy forces due to the thermal and solutal gradients are equal and opposite, both gradients being parallel and normal to gravity [from now on balanced buoyancy case (BBC)]. In this situation there is a basic conduction state even in vertical channels, slots, and rectangular cavities in general [1–6]. The first instability of this state is due to the difference of diffusivities [1, 7]. The dynamics arising from this double-diffusive instability is much richer than far from the BBC because the primary instability is subcritical [1, 2]. It can give rise to center-symmetric extended and localized steady states [4–6] and symmetry-broken steady flows with the vortices confined near the boundaries [1], depending on the length of the cavity, boundary conditions, and parameter values. Localized states were also found in the finger regime [7], but not in porous media governed by the Darcy's law [3].

Other publications [8–10] on double-diffusive convection determined the region of stability of a steady flow in a vertical channel of isothermal and impermeable lateral boundaries (see also a review in [11]). The basic flow consisted in a cubic vertical velocity field with linear distributions of the temperature and the concentration, whose amplitude may depend on the separation ratio, Se, when the Soret effect is included in the problem. They considered periodic wave perturbations traveling in the channel direction, and they mainly studied the dependence of the Grashof number on Se, on the Prandtl number, Pr, and on the wavenumber. Thermal, solutal and hydrodynamic instabilities were found in liquid mixtures of Pr = 6.7, but only the third type of instability was detected in gaseous mixtures of Pr

2

and Lewis, Le, numbers of $\mathcal{O}(1)$ [9]. On the other hand, the dependence of the thermal waves on Pr and positive Se in liquids of low Le is complex. For Se $< 0.2$ and Le $\ll 1$ there is a threshold of Pr above which they can exist, while for $0.27 <$ Se $< 0.28$ there is a gap of Pr $< 1$ where the steady flows remain stable [10]. The stability of gaseous and liquid steady flows of low Pr, in a finite slot of non-slip, impermeable and adiabatic horizontal boundaries was analyzed in [12], including the Soret coupling. The periodic flows arising from them were also computed by means of the Newton-Krylov method described in the same paper. In this case all the instabilities found were of hydrodynamic type.

The goal of the present article is to study the dynamics of a mixture of $H_2$-Xe generated by parallel gradients normal to the gravity in vertical slots, but taking into account the Soret and Dufour effects. The separation ratio and the Dufour coefficient have been obtained from experimental measures [13]. To ascertain the value of these coefficients is complex. Liu and Ahlers determined them for six binary-gas mixtures by using a combination of data from the literature, molecular-theory calculations, and thermal conductivity measurements. They concluded that the Dufour effect was weak for the mixtures analyzed [13]. The two effects were neglected in most studies (the above mentioned between them) because they are usually considered small in front of the externally imposed solutal gradients. However, the strong influence of those gradients on the temperature fluctuation in gas mixtures was already highlighted in [14] in a system where a solutal gradient instead of a temperature gradient was applied.

The importance of the Soret and Dufour effects on the bifurcation properties and patterns of convection in horizontal fluid layers heated from below has been studied since decades [15–17]. The role of the Dufour effect on the onset of convection in gases was analyzed in the first reference. The other two focus on the study of the change of the bifurcation topology at the onset of convection in liquids and gases with negative Soret couplings, and on the competition between the extended steady states and traveling waves arising below the subcritical bifurcations. In contrast, Barten *et al.* investigated the structure and dynamics of the localized traveling waves in ethanol-water mixtures with strong and weak negative Soret coupling [18]. The presence of both types of traveling waves reflected the decisive role played by the induced solutal and temperature gradients. For positive Soret couplings there is no oscillatory instability of the basic state [16].

The thermal convection in liquid binary mixtures of $^3$He-$^4$He including the Soret cou-

pling was also studied in detail in rectangular containers of large aspect ratio heated from below [19] in the range of negative separation ratios used experimentally by Kolodner [20]. They found numerically subcritical one- (waves traveling from the center of the cavity to the lateral sides), two- (blinking states), and three-frequency flows (repeated transients) from the onset of convection; the second and the third in quantitative agreement with the experiments. These flows owe their existence to the presence of the walls.

The combined effects of the Soret and Dufour coupling on binary fluid convection in a Brinkman porous horizontal layer subject to vertical fluxes of heat and mass was studied under the assumption of the existence of a basic flow parallel to the layer [21]. The study showed that the buoyancy ratio-Dufour parameter plane is divided into up to six regions, whose extension is controlled by the Soret and Dufour numbers. The influence of both effects on the Nusselt and Sherwood numbers in a porous medium was analyzed in trapezoidal geometry for different boundary conditions [22].

The critical parameters and structure of the onset of thermosolutal convection in a compressible $C_2H_6$-$CO_2$ mixture near the critical points for increasing vertical stratification was studied by Hu and Zhang [23]. In this case a thin concentration boundary layer forms along the bottom wall, which expands upwards acting as a piston and leading to a homogeneous heating of the whole fluid. The instability originates from the difference of the diffusion rates of heat and mass as in double-diffusive convection.

In the remaining of the paper, the equations and their numerical treatment are discussed in Sec. II, including the variational equations to compute stationary and periodic orbits by continuation methods, and some tests of the codes. It has been well accepted since a long time that the Dufour coupling is negligible in liquids [24], however, the existence of externally applied solutal gradients could be able to change the temperature field. Consequently, as a previous step, the products of parameters appearing in the equations for various mixtures found in the literature are evaluated to guess the need of considering these effect in the numerical models. Sec. III contains a study of the influence of the solutal gradients on the onset of the oscillatory convection in the above mentioned gas mixture. The stability of the flows is analyzed in any case, determining the bifurcation points where the periodic flows arise and the path to complex dynamics. After the discussion on the instabilities leading to periodic flows and a comparison with preceding results in Sec. IV, the paper concludes in Sec. V with a brief summary of the new dynamics observed.

## II.  MATHEMATICAL FORMULATION

The dynamics of binary mixtures filling a rectangular domain, $\Omega$, of width $d$, height $h$, and aspect ratio $\Gamma = h/d$ is numerically studied. It will be assumed that the lateral sides can diffuse mass at negligible velocity (as it can happen in rigid permeable membranes), in addition to heat. The domain is heated from the left side, and the solutal gradient is also horizontal. The top and bottom boundaries are taken impermeable and insulating. The fluid is subject to a constant vertical gravity, $\mathbf{g} = -g\mathbf{j}$, $\mathbf{j}$ being the unit vector pointing upwards. Diverse experimental setups have been used to constrain constant temperature and concentration at both lateral boundaries, see for instance those in Refs. [25, 26].

The Boussinesq approximation of the mass, momentum and energy equations is extended to that of the concentration for the denser component of the mixture. Accordingly, the density in the buoyancy force is taken as

$$\rho(\mathrm{T}^*, \mathrm{C}^*) = \overline{\rho} \left( 1 - \alpha(\mathrm{T}^* - \overline{\mathrm{T}^*}) + \beta(\mathrm{C}^* - \overline{\mathrm{C}^*}) \right), \tag{1}$$

$\alpha$ and $\beta$ being the thermal and the solutal expansion coefficients, respectively, measured at the averaged temperature $\overline{\mathrm{T}^*}$ and concentration $\overline{\mathrm{C}^*}$ at which the mean density is $\overline{\rho}$. They are defined as

$$\alpha = -\frac{1}{\overline{\rho}} \left( \frac{\partial \rho}{\partial \mathrm{T}^*} \right)_{\overline{\mathrm{T}^*}} \quad \text{and} \quad \beta = \frac{1}{\overline{\rho}} \left( \frac{\partial \rho}{\partial \mathrm{C}^*} \right)_{\overline{\mathrm{C}^*}}, \tag{2}$$

where the asterisks denote dimensional quantities. In these conditions the general equations should include the generation of internal solutal gradients due to the thermal gradients (Soret effect) and the generation of internal thermal gradients due to those of the solute (Dufour effect).

Let $x$ and $y$ be the horizontal and vertical coordinates, respectively. The system is written by splitting the dimensional temperature and concentration as

$$\mathrm{T}^*(x, y, t) = (d - x^*)\frac{\Delta \mathrm{T}^*}{d} + \mathrm{T}^*_{\mathrm{R}} + \Theta^*(x, y, t), \quad \text{and} \tag{3}$$

$$\mathrm{C}^*(x, y, t) = (d - x^*)\frac{\Delta \mathrm{C}^*}{d} + \mathrm{C}^*_{\mathrm{R}} + \Sigma^*(x, y, t), \tag{4}$$

in order to have homogeneous boundary conditions on the vertical sides. Here $\Delta \mathrm{T}^* > 0$ and $\Delta \mathrm{C}^*$ are the differences of temperature and concentration between the left and right sides, respectively, and $\mathrm{T}^*_{\mathrm{R}}$ and $\mathrm{C}^*_{\mathrm{R}}$ are the temperature and concentration on the right boundary.

5

The equations are nondimensionalized by taking $d$ as longitude scale, $\Delta \mathrm{T}^*$ as temperature scale, and $d^2/\kappa$ as time scale, $\kappa$ being the thermal diffusivity. In addition, the concentration is rescaled with $\Delta \mathrm{C}^*$, which can be greater or less than zero. Its sign determines the dynamics of the system. The nondimensional equations are

$$\boldsymbol{\nabla} \cdot \mathbf{v} = 0. \tag{5}$$

$$(\partial_t + \mathbf{v} \cdot \boldsymbol{\nabla})\mathbf{v} = -\boldsymbol{\nabla}\pi + \mathrm{Pr}\Delta\mathbf{v} - \mathrm{Ra}^{\mathrm{T}}\,\mathrm{Pr}(x - \Theta)\,\mathbf{j} + \mathrm{Ra}^{\mathrm{C}}\mathrm{Le}(x - \Sigma)\,\mathbf{j}, \tag{6}$$

$$(\partial_t + \mathbf{v} \cdot \boldsymbol{\nabla})\Theta = (1 + \mathrm{Le}\,\mathrm{Q}\,\mathrm{Se}^2)\Delta\Theta + \frac{\mathrm{Le}^2\mathrm{Q}\,\mathrm{Se}}{\mathrm{NPr}}\Delta\Sigma + u, \tag{7}$$

$$(\partial_t + \mathbf{v} \cdot \boldsymbol{\nabla})\Sigma = \mathrm{Le}\,\Delta\Sigma + (\mathrm{Pr}\,\mathrm{Se}\,\mathrm{N})\Delta\Theta + u, \tag{8}$$

where, $\mathbf{v} = (u, v)$ is the velocity field, $\mathrm{N} = \mathrm{Ra}^{\mathrm{T}}/\mathrm{Ra}^{\mathrm{C}}$ is the Rayleigh numbers ratio, $\Delta$ means the two-dimensional Laplacian and $\pi$ is the modified pressure including terms coming from the dependence of $\rho$ on T and C, and on the splitting of these magnitudes. The problem depends on six physical parameters, the thermal Rayleigh number, $\mathrm{Ra}^{\mathrm{T}}$, the solutal Rayleigh number, $\mathrm{Ra}^{\mathrm{C}}$, the Prandtl number, Pr, the Lewis number, Le, the separation ratio, Se, and the Dufour number, $Q$, defined as

$$\mathrm{Ra}^{\mathrm{T}} = \frac{\alpha g \Delta \mathrm{T}^* d^3}{\nu\kappa}, \ \mathrm{Ra}^{\mathrm{C}} = \frac{\beta g \Delta \mathrm{C}^* d^3}{D\kappa}, \ \mathrm{Pr} = \frac{\nu}{\kappa}, \ \mathrm{Le} = \frac{D}{\kappa}, \ \mathrm{Se} = \frac{\beta K_{\mathrm{T}}}{\alpha \overline{\mathrm{T}^*}}, \ \mathrm{Q} = \frac{\overline{\mathrm{T}^*}\alpha^2}{c_p\beta^2}\left(\frac{\partial\mu}{\partial\mathrm{C}^*}\right)_{\overline{p^*,\mathrm{T}^*}}, \tag{9}$$

where $\nu$ accounts for the kinematic viscosity, $D$ for the mass diffusion coefficient, $K_{\mathrm{T}}$ for the thermal diffusion ratio, $c_p$ is the specific heat at constant pressure, and $\mu$ is the chemical potential. The Rayleigh numbers will be the control continuation parameters.

In non-dimensional units $\Omega = [0,1] \times [0,\Gamma]$, and the boundary conditions can finally be written as

$$u = v = 0 \ \text{on} \ \partial\Omega \tag{10}$$

$$\Theta = 0 \ \text{on} \ x = 0,1 \quad \text{and} \quad \partial_y\Theta = 0 \ \text{on} \ y = 0,\Gamma, \tag{11}$$

$$\Sigma = 0 \ \text{on} \ x = 0,1 \quad \text{and} \quad \partial_y\Sigma = 0 \ \text{on} \ y = 0,\Gamma. \tag{12}$$

Equations (5)-(12) are rewritten in terms of the streamfunction, $\psi$, related with the

velocity field by $\mathbf{v} = (\partial_y \psi, -\partial_x \psi)$. They become

$$\partial_t \Delta \psi + J(\Delta \psi, \psi) = \text{Pr} \Delta^2 \psi + \text{Ra}^{\text{T}} \text{Pr} \,(1 - \partial_x \Theta) - \text{Ra}^{\text{C}} \text{Le} \,(1 - \partial_x \Sigma), \tag{13}$$

$$\partial_t \Theta + J(\Theta, \psi) = (1 + \text{Le Q Se}^2)\Delta\Theta + \frac{\text{Le}^2 \text{Q Se}}{\text{NPr}}\Delta\Sigma + \partial_y \psi, \tag{14}$$

$$\partial_t \Sigma + J(\Sigma, \psi) = \text{Le}\,\Delta\Sigma + \text{Pr SeN}\Delta\Theta + \partial_y \psi, \tag{15}$$

where $J(f, h) = \partial_x f \partial_y h - \partial_y f \partial_x h$. In this way the incompressibility condition is identically fulfilled, and the number of unknowns is reduced. The boundary conditions for $u$ and $v$ translate into

$$\psi = \partial_n \psi = 0 \ \text{ on } \ \partial\Omega, \tag{16}$$

where $n$ indicates the normal direction to the boundary.

Equations (13)-(15) together with boundary conditions (11), (12), and (16) are $\mathcal{Z}_2$ equivariant, i.e., they remain invariant under the center symmetry

$$\mathcal{S} : (t, x, y, \psi, \Theta, \Sigma) \to (t, 1 - x, \Gamma - y, \psi, -\Theta, -\Sigma). \tag{17}$$

Equations (7)-(8) show that the relevance of the Soret and Dufour effects depends on the solutal gradient in inverse form, i.e., large solutal gradients could enhance the Dufour and weaken the Soret effects for a fixed differential thermal gradient (see parameter N in the equations). An estimation of the contribution of the Dufour and Soret coefficients to the dynamics of several fluids through the coefficients $\text{Le}^2 \text{Q Se/NPr}$ and $\text{Pr SeN}$, respectively, can be seen in Table I. The data on the mixtures were extracted from several sources, despite it is difficult to find complete sets of physical coefficients for liquid mixtures in the literature. The Dufour and Soret effects also give an additional contribution to the heat diffusion via $\text{Le Q Se}^2$, which is independent of the buoyancies. Despite it is well known that $Q$ is usually very small in liquids, the product of the coefficients is calculated to see if large externally applied solutal gradients could be able to change the transport properties of the liquid mixtures and to increase their influence in gases. Three main conclusions can be extracted *a priori* from the table. The enhance of the diffusion of the temperature $(\text{Le Q Se}^2)$ is only important in gases, for which $Q$ can be large. Moreover, the Dufour effect appears to be important for liquid metals in extreme conditions as those that exist in the Earth's liquid core at very large Lewis numbers (see last row of the table). On the other hand, the

7

TABLE I. Values of the parameters taken from experimental works or estimated from physical coefficients extracted from different sources when possible, and the products which appear in the terms of Eqs. (14) and (15). Realistic values taken ad-hoc, and based on the corresponding source are printed in bold format. The Dufour coefficients are taken $10^{-5}$ in order to compare the products when $Q$ is neglected in the literature, then the coefficient could be underestimated. In the first two rows BGM means binary gas model. The four last rows correspond to liquid metals at high pressure and temperature. The concentrations vary in each mixture.

| Source | Mixture | Pr | Le | Se | $Q$ | N | Pr SeN | Le$^2$Q Se/NPr | Le Q Se$^2$ |
|---|---|---|---|---|---|---|---|---|---|
| [17] | BGM | 1. | 1. | −0.5 | 10 | 1 | −0.5 | −5.0 | 2.5 |
| [17] | BGM | 1. | 1. | −0.5 | 10 | 0.25 | −0.125 | −20.0 | 2.5 |
| [13] | Ar-CO$_2$ | 0.683 | 1.085 | 0.0032 | 37.82 | 1 | $2.186 \times 10^{-3}$ | $2.086 \times 10^{-1}$ | $4.202 \times 10^{-4}$ |
| [13] | Ar-CO$_2$ | 0.683 | 1.085 | 0.0032 | 37.84 | 0.25 | $5.464 \times 10^{-4}$ | $8.344 \times 10^{-1}$ | $4.202 \times 10^{-4}$ |
| [13] | H$_2$-Xe | 0.168 | 1.238 | 0.232 | 0.357 | 1 | $3.898 \times 10^{-2}$ | $7.556 \times 10^{-1}$ | $2.379 \times 10^{-2}$ |
| [13] | H$_2$-Xe | 0.168 | 1.238 | 0.232 | 0.357 | 0.25 | $9.744 \times 10^{-3}$ | 3.0224 | $2.379 \times 10^{-2}$ |
| [15] | C$_2$H$_6$O-H$_2$O | 7. | 0.01 | **−0.25** | 0.1 | 1 | −1.75 | $-3.571 \times 10^{-7}$ | $6.25 \times 10^{-5}$ |
| [15] | C$_2$H$_6$O-H$_2$O | 7. | 0.01 | **−0.25** | 0.1 | 0.25 | $-4.375 \times 10^{-1}$ | $-1.429 \times 10^{-6}$ | $6.25 \times 10^{-5}$ |
| [27] | DNA-H$_2$O | 10 | $10^{-4}$ | **−0.01** | **$10^{-5}$** | 1 | $1.0 \times 10^{-1}$ | $-1.0 \times 10^{-16}$ | $1.0 \times 10^{-13}$ |
| [27] | DNA-H$_2$O | 10 | $10^{-4}$ | **−0.01** | **$10^{-5}$** | 0.25 | $-2.5 \times 10^{-2}$ | $-4.0 \times 10^{-16}$ | $1.0 \times 10^{-13}$ |
| [28] | C$_2$H$_6$O-H$_2$O | 30.97 | 0.0049 | 0.2 | **$10^{-5}$** | 1 | 6.194 | $1.551 \times 10^{-12}$ | $1.960 \times 10^{-9}$ |
| [28] | C$_2$H$_6$O-H$_2$O | 30.97 | 0.0049 | 0.2 | **$10^{-5}$** | 0.25 | 1.549 | $6.202 \times 10^{-12}$ | $1.960 \times 10^{-9}$ |
| [29] | $^3$He-$^4$He | 0.707 | 0.076 | −0.098 | **$10^{-5}$** | 1 | $-6.929 \times 10^{-2}$ | $-8.006 \times 10^{-9}$ | $7.299 \times 10^{-9}$ |
| [29] | $^3$He-$^4$He | 0.707 | 0.076 | −0.098 | **$10^{-5}$** | 0.25 | $-1.732 \times 10^{-2}$ | $-3.203 \times 10^{-8}$ | $7.299 \times 10^{-9}$ |
| [30] | Fe-Si-O | 0.046 | 300 | **$10^{-3}$** | **$10^{-5}$** | 1 | $4.6 \times 10^{-5}$ | $1.9565 \times 10^{-2}$ | $3.000 \times 10^{-9}$ |
| [30] | Fe-Si-O | 0.046 | 300 | **$10^{-3}$** | **$10^{-5}$** | 0.25 | $1.15 \times 10^{-5}$ | $7.826 \times 10^{-2}$ | $3.000 \times 10^{-9}$ |

dilute organic or inorganic mixtures in water give negligible Dufour and extra diffusion term effects. They could only be relevant with extremely high values of N.

To obtain the numerical solutions, the functions $\psi$, $\Theta$ and $\Sigma$ were approximated by a pseudo-spectral collocation method on a mesh of $n_x \times n_y$ Gauss-Lobatto points. The system was discretized by transforming the spatial operators into matrices acting on the values of the functions at the collocation mesh points. The momentum equation was solved

following the algorithm for the vorticity-streamfunction formulation described in Ref. [31]. The stiff system of ODEs obtained after the spatial discretization is integrated by means of an implicit-explicit (IMEX) fifth-order BDF-extrapolation method.

The computation of stationary and periodic orbits by continuation methods and the stability of the flows [12, 32–34] requires solving the first variational equations of system (13-15), which depend on the parameter, p, used in the continuation. The methods and the advantages of their use are described in detail in [12]. Only the parameter $p = Ra^T$ is used in this study, then these equations for the perturbations $(\psi_1, \Theta_1, \Sigma_1)$, and $\delta Ra^T$ are

$$\partial_t \Delta \psi_1 + J(\Delta \psi_1, \psi) + J(\Delta \psi, \psi_1) = Pr \Delta^2 \psi_1 - Ra^T Pr \, \partial_x \Theta_1 - Ra^C Le \, \partial_x \Sigma_1 +$$
$$+ \delta Ra^T Pr(1 - \partial_x \Theta) \tag{18}$$

$$\partial_t \Theta_1 + J(\Theta_1, \psi) + J(\Theta, \psi_1) = (1 + Le \, Q \, Se^2) \Delta \Theta_1 + \frac{Le^2 Q \, Se}{N \, Pr} \Delta \Sigma_1 -$$
$$- \delta Ra^T \frac{Le^2 Q \, Se}{Ra^T N \, Pr} \Delta \Sigma + \partial_y \psi_1, \tag{19}$$

$$\partial_t \Sigma_1 + J(\Sigma_1, \psi) + J(\Sigma, \psi_1) = Le \Delta \Sigma_1 + N \, Pr \, Se \Delta \Theta_1 + \delta Ra^T \frac{Pr \, Se}{Ra^C} \Delta \Theta + \partial_y \psi_1, \tag{20}$$

with boundary conditions

$$\psi_1 = \partial_n \psi_1 = 0 \text{ on } \partial \Omega. \tag{21}$$

$$\Theta_1 = 0 \text{ on } x = 0, 1 \quad \text{and} \quad \partial_y \Theta_1 = 0 \text{ on } y = 0, \Gamma, \tag{22}$$

$$\Sigma_1 = 0 \text{ on } x = 0, 1 \quad \text{and} \quad \partial_y \Sigma_1 = 0 \text{ on } y = 0, \Gamma. \tag{23}$$

The variational equations for other parameters are included in the Appendix.

Some preliminary calculations to decide the resolution used in the computations have been done. Table II shows the leading eigenvalue, $\lambda^1$, or multiplier, $\mu^1$, the period, $T$, the averaged kinetic energy, $\overline{K}$, the Nusselt, $\overline{\partial_x T}$, and Sherwood, $\overline{\partial_x C}$, numbers calculated at $x = 1$, obtained from the numerical calculation of some steady states (SS) and periodic orbits (PO), and their stability. The averages are defined as

$$\overline{\partial_x T} = \frac{1}{\Gamma} \int_t^{t+T} \int_0^\Gamma \partial_x T \, dy \, dt, \quad \text{and} \quad \overline{\partial_x C} = \frac{1}{\Gamma} \int_t^{t+T} \int_0^\Gamma \partial_x C \, dy \, dt,, \tag{24}$$

and

$$\overline{K} = \frac{1}{2\Omega} \int_t^{t+T} \int_\Omega \mathbf{v} \cdot \mathbf{v} \, d\Omega \, dt. \tag{25}$$

9

TABLE II. Comparison of the real and imaginary parts of the leading eigenvalue $\lambda^1$ or multiplier $\mu^1$ of the spectrum, the period, the averaged kinetic energy density, and the averaged heat and mass transfer for steady states (SS) and periodic orbits (PO). The rest of parameters are $\mathrm{Pr} = 0.1$, $\mathrm{Le} = 0.05$, $\mathrm{Se} = -0.05$, $Q = 0$, and $\Gamma = 8$.

| $n_x \times n_y$ | Type | $\mathrm{Ra^T}$ | $\mathrm{Ra^C}$ | $\Re(\lambda^1)$ | $\Im(\lambda^1)$ | $T$ | $\overline{K}$ | $\overline{\partial_x \mathrm{T}}$ | $\overline{\partial_x \mathrm{C}}$ |
|---|---|---|---|---|---|---|---|---|---|
| $32 \times 128$ | SS | 3000 | 1500 | 0.09326 | $\pm 6.8267$ | $--$ | 31.52452 | 1.27922 | 3.25614 |
| $32 \times 128$ | SS | 13500 | $-13500$ | $-0.6412$ | 0 | $--$ | 209.2510 | 1.97451 | $-5.4444$ |
| $40 \times 150$ | SS | 3000 | 1500 | 0.09295 | $\pm 6.8271$ | $--$ | 31.52445 | 1.27922 | 3.25612 |
| $40 \times 150$ | SS | 13500 | $-13500$ | $-0.6735$ | 0 | $--$ | 209.2763 | 1.97459 | $-5.4452$ |
| $50 \times 200$ | SS | 3000 | 1500 | 0.09298 | $\pm 6.8270$ | $--$ | 31.52447 | 1.27922 | 3.25612 |
| $50 \times 200$ | SS | 13500 | $-13500$ | $-0.6606$ | 0 | $--$ | 209.1953 | 1.97458 | $-5.44742$ |
| $n_x \times n_y$ | Type | $\mathrm{Ra^T}$ | $\mathrm{Ra^C}$ | $\Re(\mu^1)$ | $\Im(\mu^1)$ | $T$ | $\overline{K}$ | $\overline{\partial_x \mathrm{T}}$ | $\overline{\partial_x \mathrm{C}}$ |
| $32 \times 128$ | PO | 3500 | $-7000$ | 0.72878 | 0 | 0.607692 | 85.1235 | 1.37477 | $-4.15034$ |
| $32 \times 128$ | PO | 4500 | 2250 | 0.65904 | 0 | 0.713853 | 50.0377 | 1.39613 | 3.65151 |
| $40 \times 150$ | PO | 3500 | $-7000$ | 0.72894 | 0 | 0.607694 | 85.1230 | 1.37476 | $-4.15037$ |
| $40 \times 150$ | PO | 4500 | 2250 | 0.65947 | 0 | 0.713827 | 50.0388 | 1.39614 | 3.65159 |
| $50 \times 200$ | PO | 3500 | $-7000$ | 0.72897 | 0 | 0.607691 | 85.1227 | 1.37476 | $-4.15036$ |
| $50 \times 200$ | PO | 4500 | 2250 | 0.65941 | 0 | 0.713825 | 50.0384 | 1.39613 | 3.65154 |

The integral over time only applies for the periodic orbits. Then $T$ is the period.

As can be seen a mesh of $n_x \times n_y = 40 \times 150$ is sufficient in the interval of Ra considered to have errors less than 0.5% in the values of the eigenvalues and multipliers and less in the averaged quantities.

## III. INFLUENCE OF THE SOLUTAL GRADIENT ON THE ONSET OF THE OSCILLATORY FLOWS

In order to study the influence of the concentration on the dynamics of the steady and time periodic double-diffusive fluids subjects to externally added solutal gradients the $H_2$-Xe gas mixture of molar mass ratio 65.1 listed in Table I was selected because the parameters are well determined [13], and the separation ratio and Dufour coefficients have a similar

weight. The aspect ratio of the slot was fixed to $\Gamma = 8$, large enough to allow a rich variety of solutions. Five cases with different $\text{Ra}^{\text{C}}$ were selected. It was found that for any of them the initial steady flow is center-symmetric, i.e., it is invariant by $\mathcal{S}$ like with impermeable lateral sides [12]. Consequently, it fulfills

$$\psi(t, 1 - x, \Gamma - y) = \psi(t, x, y), \tag{26}$$

$$\Theta(t, 1 - x, \Gamma - y) = -\Theta(t, x, y), \tag{27}$$

$$\Sigma(t, 1 - x, \Gamma - y) = -\Sigma(t, x, y), \tag{28}$$

and the velocity field fulfills

$$u(t, 1 - x, \Gamma - y) = -u(t, x, y), \tag{29}$$

$$v(t, 1 - x, \Gamma - y) = -v(t, x, y). \tag{30}$$

## A.   Dynamics with a negligible solutal gradient

The first case, shown in Fig. 1 is computed with a negligible solutal gradient ($\text{Ra}^{\text{C}} = 1.0$). Figures 1(a), (b) show the Nusselt number versus $\text{Ra}^{\text{T}}$, and Fig. 1(c), (d) the period of the PO also versus $\text{Ra}^{\text{T}}$. The Nusselt number increases monotonically with $\text{Ra}^{\text{T}}$ in the steady regime. It becomes unstable at $\text{Ra}^{\text{T}} = 2858.7$ through a supercritical Hopf bifurcation (HB). The emerging periodic orbits are fixed cycles, i.e., they are center-symmetric at any time instant. The next critical point along the branch of steady solutions is found at a much higher $\text{Ra}^{\text{T}} = 12410$. The critical eigenfunction is real, and in this case the center symmetry is broken. This pitchfork bifurcation gives rise to unstable steady flows from the beginning, which have not been continued.

The periodic flow arising at the HB (see detail in Fig. 1(b)) becomes unstable at $\text{Ra}^{\text{T}} = 4030.7$ in a period-doubling (PD) bifurcation, and neither the steady nor the periodic flow recover stability, at least in the calculated range of parameters (black and red curves in Fig. 1). By increasing the parameter the already unstable periodic branch has another PD bifurcation at $\text{Ra}^{\text{T}} = 8215.1$ when a second multiplier becomes unstable without breaking the symmetry. The branch arising from this point is extremely unstable. The leading multiplier has modulus $1.357 \times 10^5$, so computing the branch does not give information on new stable flows. Finally there is a pitchfork bifurcation of periodic orbits (PPO) at $\text{Ra}^{\text{T}} = 9006.6$
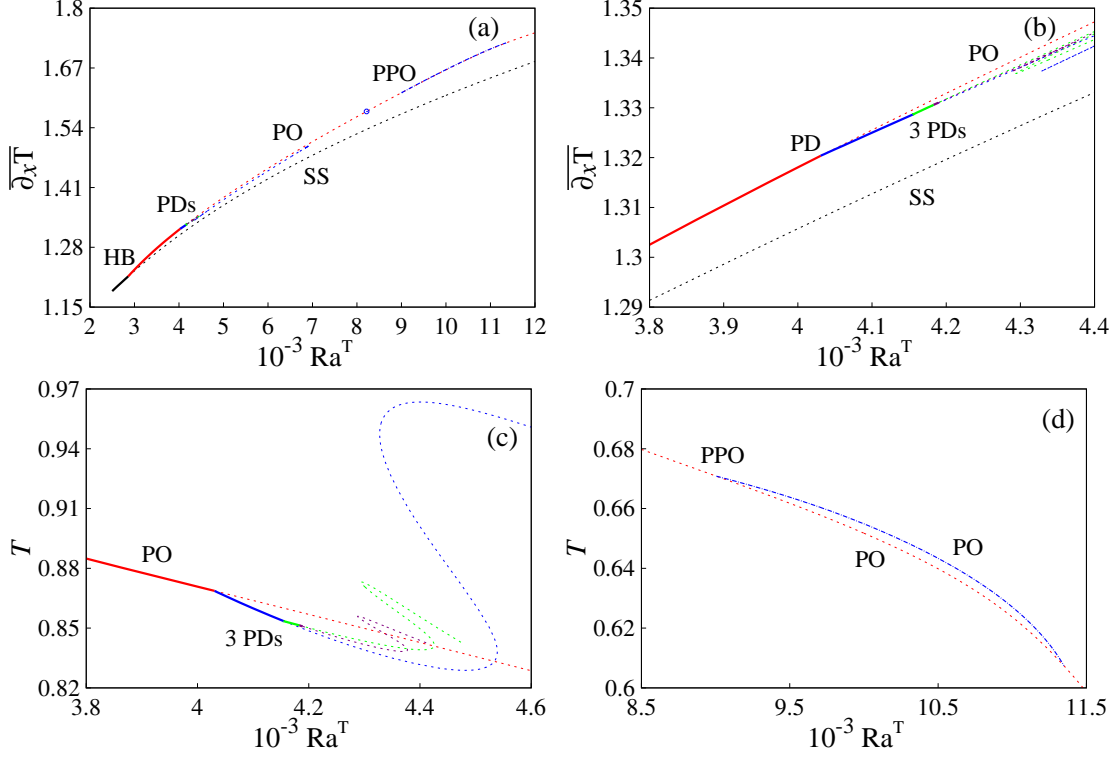
FIG. 1. (a) Nusselt number versus $Ra^T$ for $Ra^C = 1.0$. The solid lines indicate stable solutions and the dashed lines the unstable ones. Black color lines mean steady states (SS), red, blue, green and purple lines denote time periodic orbits (PO), and the blue dash-dotted line refers to unstable PO. In addition, HB means Hopf bifurcation, PPO signifies pitchfork bifurcation of PO, and PD means period-doubling. (b) detail of (a) showing orbits arising at the PD points and the double fold of the first double-period orbit, (c) shows the period $T$, $T/2$, $T/4$ and $T/8$ of the PO versus $Ra^T$, and (d) the period $T$ of the asymmetric PO.

when a third real multiplier crosses the unit circle, breaking the center symmetry. At this point the first multiplier has modulus $4.735 \times 10^2$, so the first time dependent orbit is very unstable.

The flows of double period [see Fig. 1(b)] lose stability at $Ra^T = 4155.1$ in a second PD bifurcation. By increasing the parameter, the curve of double-period solutions has a double fold at $Ra^T = 4539.0$ and at $Ra^T = 4327.5$ [see Fig. 1(c)] when the same real multiplier crosses forth and back the unit circle. It remains unstable from $Ra^T = 4328.8$. At $Ra^T = 6671.5$ the leading multiplier is $1.063 \times 10^4$ and it grows with $Ra^T$, therefore following this branch is also too expensive and unnecessary. The new branches of quadruple- and

12
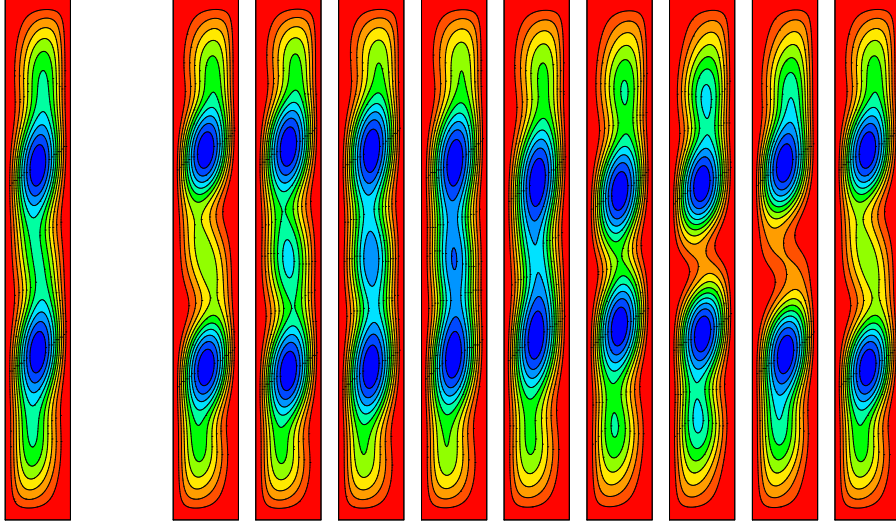
FIG. 2. Contour plots of the streamfunction of a stable steady flow for $\mathrm{Ra}^{\mathrm{T}} = 2500$ at left, and of the temporal evolution of a stable periodic orbit during a period $T = 0.90593$ for $\mathrm{Ra}^{\mathrm{T}} = 3518.3$ at right. The snapshots are taken in time intervals $\Delta t = T/8$. $\mathrm{Ra}^{\mathrm{C}} = 1$.

subsequent octuple-period orbits are supercritical, and lose their stability at $\mathrm{Ra}^{\mathrm{T}} = 4183.1$ and $\mathrm{Ra}^{\mathrm{T}} = 4189.2$, respectively, in new PDs. The estimation of the Feigenbaum constant

$$\delta = \lim_{n \to \infty} \frac{a_{n-1} - a_{n-2}}{a_n - a_{n-1}}$$

with just $n = 3$ gives $\delta = 4.401$, and with $n = 4$ already gives $\delta = 4.567$, pointing out that the next bifurcations give rise to a Feigenbaum cascade. The terms of the sequence, $a_n$, are the successive critical $\mathrm{Ra}^{\mathrm{T}}$. Figures 1(b) and (c) show the shortening of the stable part of the branches of PO between PDs as $\mathrm{Ra}^{\mathrm{T}}$ increases. Figure 1(c) also displays the double folds of the other two branches after each period doubling.

Figures 2, 3, and 4 show the contour plots of the streamfunction of a steady solution on the primary branch and of the temporal evolution of a bifurcated periodic orbit, of a double-period orbit, and of a quadruple-period orbit, respectively. All these flows are center-symmetric. The primary steady solutions have two vortices (left contour plot in Fig. 2) that when the flow becomes periodic (right part of Fig. 2), travel to the center of the slot, and again to the horizontal boundaries to get back to the initial position. When they reach the maximum distance a weak vortex develops between them. The flows after the successive PDs behave basically in the same way. The vertical oscillation simply occurs twice, four, eight, etc. times in a period. In these and all subsequent color contour plots the minimum

13
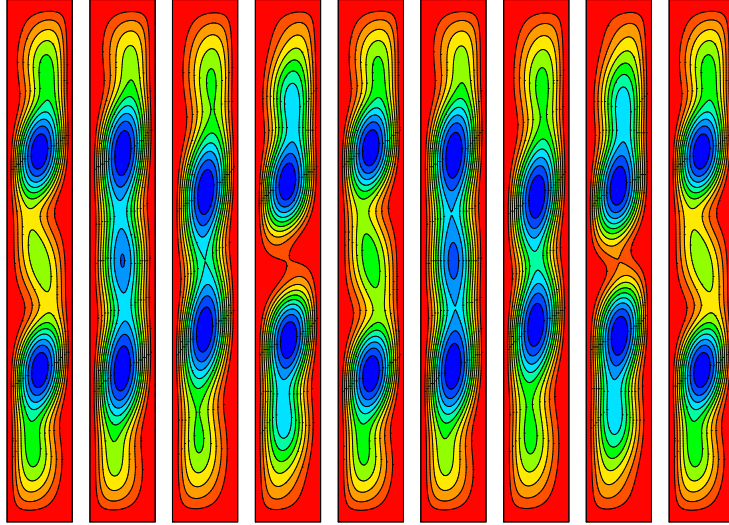
FIG. 3. Idem Fig. 2 for the stable time periodic orbit of double period at $Ra^T = 4061.1$, with $T = 1.7295$. $Ra^C = 1$.
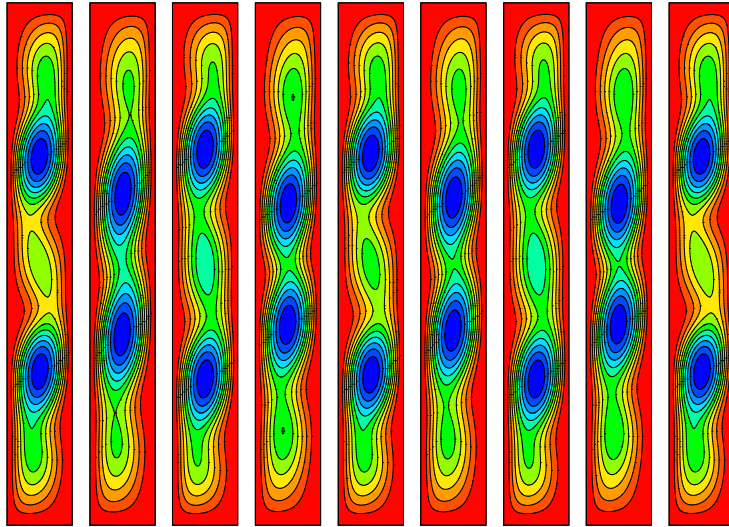


FIG. 4. Idem Fig. 2 for the stable time periodic orbit of quadruple period at $Ra^T = 4168.7$, with $T = 3.4098$. $Ra^C = 1$.

value of the represented function is in blue and the maximum in red. Therefore, in the case of the streamfunction, vortices with a blue (red) core rotate clockwise (counterclockwise), and a red (blue) color close to the boundary indicates a global clockwise (counterclockwise) circulation.

Figure 5 shows the contour plots of the temporal evolution of a periodic flow with broken symmetry during a period. In this case the two vortices travel to the center of the slot while
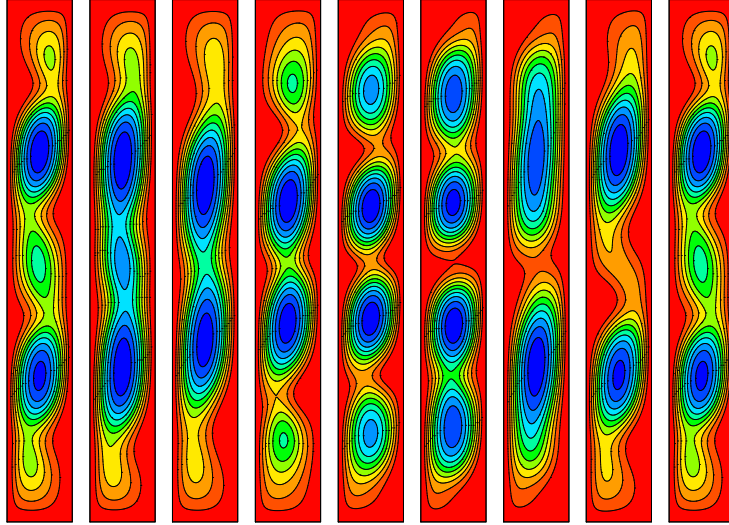
FIG. 5. Idem Fig. 2 for the unstable time periodic orbit with broken symmetry at $\mathrm{Ra}^{\mathrm{T}} = 9996.6$, with $T = 0.65495$. $\mathrm{Ra}^{\mathrm{C}} = 1$.

new vortices appear near the horizontal sides, then they elongate and reconnect in pairs, recovering the initial position, size and shape with a weak vortex between them.

## B. Dynamics near the BBC

Figure 6 shows the bifurcation diagram for $\mathrm{Ra}^{\mathrm{C}} = 1750$. The primary branch of SS and its stability are computed in the interval $[1, 40000]$. This branch of center-symmetric solutions turns back and forth twice reaching very low $\mathrm{Ra}^{\mathrm{T}}$. All the bifurcations on the diagram are steady, giving rise to folds, or pitchfork bifurcations if the critical eigenvector breaks the center symmetry. The sequence of bifurcations found can be followed in Fig. 6 (black lines), and in Table III, which contains the intervals between bifurcations with the number of unstable eigenvalues. From now on, the term saddle-node will only be used to refer to bifurcation points at which two solutions collide and disappear, one of them being stable and the other unstable. When both are unstable the general terms fold or turning points will be used.

By following the curve of solutions, starting from the left, the steady flow is stable up to $\mathrm{Ra}^{\mathrm{T}} = 11844$ (see details in Figs. 6(b) and (c)). At this point there is a pitchfork bifurcation (P1) of equilibria breaking the center symmetry of the initial solution (the critical eigenfunction is antisymmetric). Next, the curve turns back in the small loop of Fig. 6(b)

when a second eigenvalue becomes unstable at $\mathrm{Ra}^{\mathrm{T}} = 12005$ (T1). From this point the curve undergoes two more tiny turning points, with a pitchfork bifurcation (P2) between them, before continuing to lower $\mathrm{Ra}^{\mathrm{T}}$. The second fold takes place at $\mathrm{Ra}^{\mathrm{T}} = 11804$ (T2) when a third real eigenvalue crosses the imaginary axis. Next, a real positive eigenvalue becomes stable at $\mathrm{Ra}^{\mathrm{T}} = 11813$ in P2 [see Fig. 6(b)]. The same holds at the third turning point of the curve at $\mathrm{Ra}^{\mathrm{T}} = 11822$ (T3). After the sequence of folds, one eigenvalue remains positive. The next pitchfork bifurcation takes place when a second real eigenvalue becomes positive at $\mathrm{Ra}^{\mathrm{T}} = 6504.2$ (P3) before $\mathrm{Ra}^{\mathrm{T}}$ decreases down to a turning point at $\mathrm{Ra}^{\mathrm{T}} = 4896.5$ (T4) [see Fig. 6(d)]. Here a third real eigenvalue becomes positive.

Following the curve to high $\mathrm{Ra}^{\mathrm{T}}$ another pitchfork bifurcation is found at $\mathrm{Ra}^{\mathrm{T}} = 11217$ (P4), closely followed by another turning point at $\mathrm{Ra}^{\mathrm{T}} = 11594$ (T5) (see Figs. 6(b) and (d)). After the two latter steady bifurcations three real eigenvalues remain positive. A new pitchfork bifurcation is found on the curve at $\mathrm{Ra}^{\mathrm{T}} = 11593$ (P5) when the third eigenvalue stabilizes. By decreasing $\mathrm{Ra}^{\mathrm{T}}$ the curve turns up again at $\mathrm{Ra}^{\mathrm{T}} = 6496.9$ (T6) in another fold [see Fig. 6(e)], and only a real eigenvalue remains positive. At $\mathrm{Ra}^{\mathrm{T}} = 6819.1$ (P6) it becomes negative, and the steady solution becomes stable up to a saddle-node bifurcation at $\mathrm{Ra}^{\mathrm{T}} = 12212$ (S7) [see Fig. 6(b)], and the flow loses the stability again. Between P6 and S7 there is large range of parameters with two stable steady flows (see Fig. 6(a), and the contour plots below).

Between S7 and the next saddle-node (S8) in which the curve turns to higher $\mathrm{Ra}^{\mathrm{T}}$ there are two very close pitchfork bifurcations that leave just one positive eigenvalue [see Fig. 6(b)]. The critical pitchfork points are at $\mathrm{Ra}^{\mathrm{T}} = 12202$ (P7) and $\mathrm{Ra}^{\mathrm{T}} = 12157$ (P8), and S8 is placed at $\mathrm{Ra}^{\mathrm{T}} = 12153$, where the curve stabilizes up to a new saddle-node point placed at $\mathrm{Ra}^{\mathrm{T}} = 11266$ (S9) [see Fig. 6(f) and (g)]. The last critical saddle-node found is located at $\mathrm{Ra}^{\mathrm{T}} = 12651$ (S10), where the flow becomes stable up to the end of the interval of $\mathrm{Ra}^{\mathrm{T}}$ computed. Between S9 and S10 there are two pitchfork bifurcations (P9 and P10), which are extremely close to S9 and S10 respectively [see Fig. 6(g)]. Their positions differ in the ninth or tenth significant digit, very close to, or at a double-zero point.

The minimum of the curve occurs at $\mathrm{Ra}^{\mathrm{T}} = 12896$ (C) that fulfills the condition $\mathrm{Ra}^{\mathrm{T}} \mathrm{Pr} = \mathrm{Ra}^{\mathrm{C}} \mathrm{Le}$. In this case there is a conduction state in which $\Theta = 0$, $\Sigma = 0$, and the fluid is at rest. If this condition is kept by increasing simultaneously $\mathrm{Ra}^{\mathrm{T}}$ and $\mathrm{Ra}^{\mathrm{C}}$ from a small value, the conduction state is stable up to a critical point. This case was studied in [1, 4]

TABLE III. Values of $Ra^T$ and number of eigenvalues with positive real part (PRPE) in the segments between the critical points labeled on the bifurcation diagram of Fig. 6 for $Ra^C = 1750$. The other parameters are Pr = 0.168, Le = 1.238, Se = 0.232, $Q = 0.357$, and $\Gamma = 8$ are kept constant. B means beginning of the calculations done ($Ra^T = 1$).

| Segment | $Ra^T$ | PRPE | Segment | $Ra^T$ | PRPE |
|---|---|---|---|---|---|
| B-P1 | $1.000 - 11844$ | 0 | T6-P6 | $6496.9 - 6819.1$ | 1 |
| P1-T1 | $11844 - 12005$ | 1 | P6-S7 | $6819.1 - 12212$ | 0 |
| T1-T2 | $12005 - 11804$ | 2 | S7-P7 | $12212 - 12202$ | 1 |
| T2-P2 | $11804 - 11813$ | 3 | P7-P8 | $12202 - 12157$ | 2 |
| P2-T3 | $11813 - 11822$ | 2 | P8-S8 | $12157 - 12153$ | 1 |
| T3-P3 | $11822 - 6504.2$ | 1 | S8-S9 | $12153 - 12662$ | 0 |
| P3-T4 | $6504.2 - 4896.5$ | 2 | S9-P9 | $12662 - 12662$ | 1 |
| T4-P4 | $4896.5 - 11217$ | 3 | P9-P10 | $12662 - 12651$ | 2 |
| P4-T5 | $11217 - 11594$ | 4 | P10-S10 | $12651 - 12651$ | 1 |
| T5-P5 | $11594 - 11593$ | 3 | S10-HB | $12651 - 39167$ | 0 |
| P5-T6 | $11593 - 6496.9$ | 2 | | | |

with periodic boundary conditions. Consequently, the curve passes through the conduction state at which Nu = 1 and $K = 0$ [see Fig. 6(h)]. At this point the global anticlockwise flow changes to clockwise. A flow evolving cyclically from clockwise to counterclockwise and vice versa was found in double-diffusive convection in a square enclosure with applied vertical solute and heat gradients [35], but no similar dynamics has been found in the present study near the point C. Finally, the steady flow loses stability at $Ra^T = 39167$ in a supercritical HB of period 0.17208, which does not break the symmetry of the steady flow.

Figure 7 shows the contour plots of the solutions on the primary branch to see how the different stable steady flows develop. Their location is marked with a black cross on the details of Fig. 6, but the first and the last are out of the window shown. Those stable are on the solid lines. At low $Ra^T$ the flow consists of three equidistant vortices. Following the curve to the right the vortices shrink and the central one weakens and lengthens in the folds of the loop of Fig. 7(b). The latter splits forming two new vortices of increasing intensity by decreasing $Ra^T$. The four vortices already have the same intensity before T4
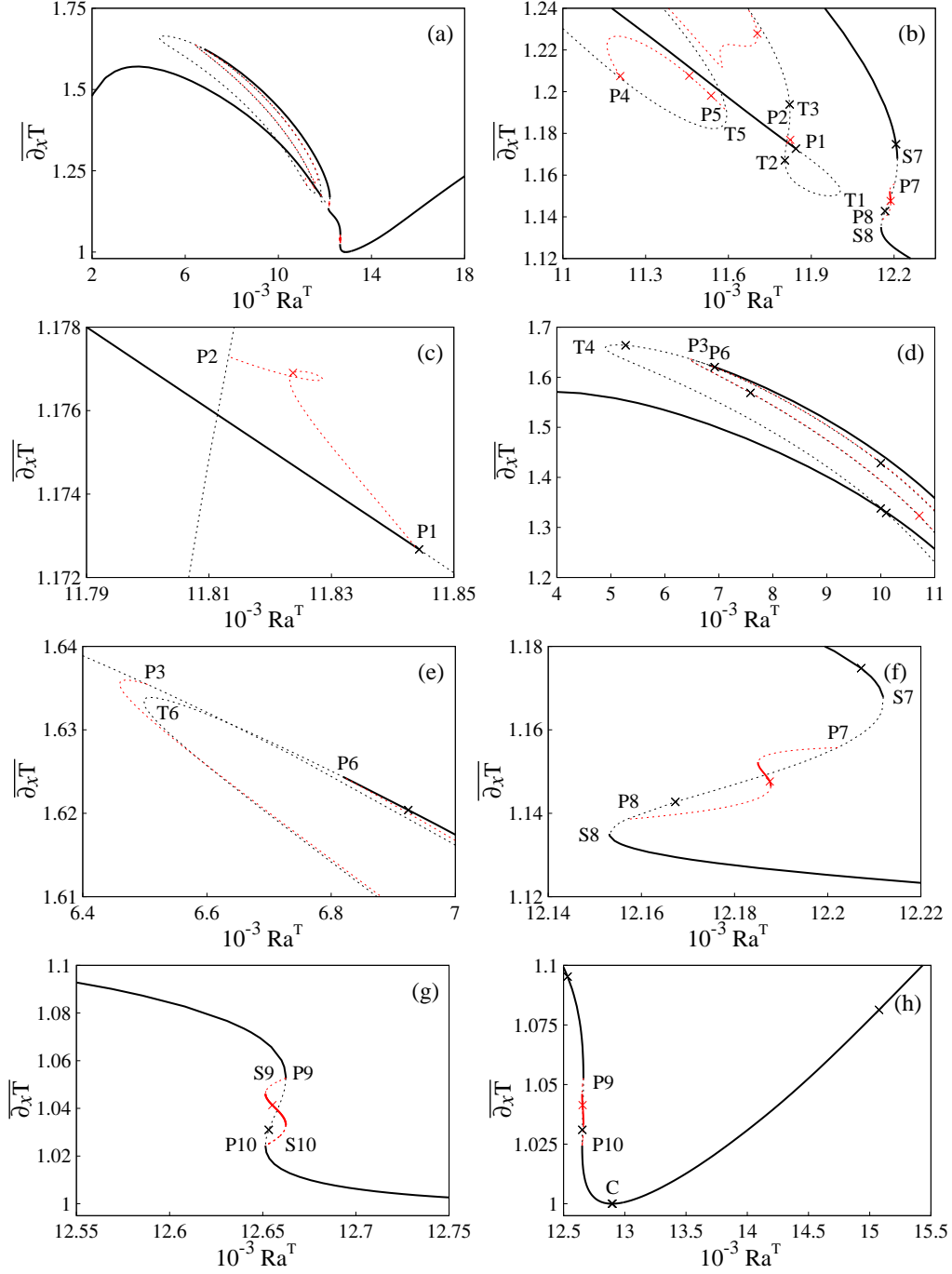
FIG. 6. Idem Fig. 1 for $Ra^C = 1750$. (a) Full diagram, and from (b) to (h) details of (a) showing the bifurcations on the curve of the primary flow and the secondary steady flows in red. TI, with $I = 1, \cdots, 6$, indicate turning points, SI, with $I = 7, \cdots, 10$, indicate saddle-node bifurcations of equilibria, PI, with $I = 1, \cdots, 10$, label the pitchfork bifurcations of steady solutions, and C indicates the conduction state. All the labels belong to the main branch. The crosses indicate the position of the solutions shown in Figs. 7 to 10.

18

[see Fig. 7(d)]. After T4 the four-vortex solutions remain unstable, changing slightly at T5 and T6, and stabilizing past P6. One of these solutions is shown in the first column of the second row of contour plots and signaled in Figs. 7(d) and 7(e). By following the stable part of the curve the central vortices weaken and disappear remaining only two boundary vortices, which are stable between the saddle-nodes S8 and S9 of Figs. 7(f) and 7(g) (see the upper left corner of Fig. 7(h) for locating the point drawn). Next, the two vortices elongate and join forming a big vortex near the minimum of the curve (C). Two nearby solutions are shown there, one at each side of the BBC point [see Fig. 7(h)]. The change of color of the contour plots indicates the change from the counterclockwise to the clockwise direction of circulation. Finally, the vortex contracts forming an elongated one in the center of the slot, which remains stable until the HB. Only two weak vortices above and below the central one appear when the parameter is very high. The stable branch of center-symmetric periodic orbits soon becomes unstable in a saddle-node bifurcation at $\mathrm{Ra}^\mathrm{T} = 39762$. The dynamics of the periodic orbits near the bifurcation point simply consists in the slight intensification and weakening of the outer vortices. The next transition on the unstable branch of periodic orbits is a PD bifurcation, with the -1 multiplier decreasing very fast when $\mathrm{Ra}^\mathrm{T}$ decreases.

Figure 8 shows the superposition of the contour plots of the concentration and the velocity field at the same points as those shown for the streamfunction. Like for the temperature (not shown) the fluid is pulled from the sides following the vortices so that the concentration inside the cavity form a sinusoidal profile, which depends on the number, position and strength of the vortices. The concentration is almost a linear $x$-function when the vortices are confined near the horizontal sides.

The secondary curves are plotted in red color. In all cases they join pairs of pitchfork points. The curves joining P1-P2, P4-P5, and P3-P6 are always unstable, and the bifurcations along them are the folds shown in Figs. 6(c), (b) and (d) respectively. The curves P7-P8 and P9-10 undergo saddle-node points [see Figs. 6 (f) and (g)]. The difference between them is the location of the pitchfork bifurcations. In the second case the curve goes practically from S9 to S10. The first saddle-node on the secondary curves stabilizes the fluid, and the second destabilizes it. Therefore, in two small regions the steady antisymmetric flows are stable. Specifically, in the first case the flow is stable between $\mathrm{Ra}^\mathrm{T} = 12185$, which is the first saddle-node on the red curve after P7, and $\mathrm{Ra}^\mathrm{T} = 12188$, which is the second before P8. In the second case, the saddle-nodes on the secondary curve giving the range of stability

19
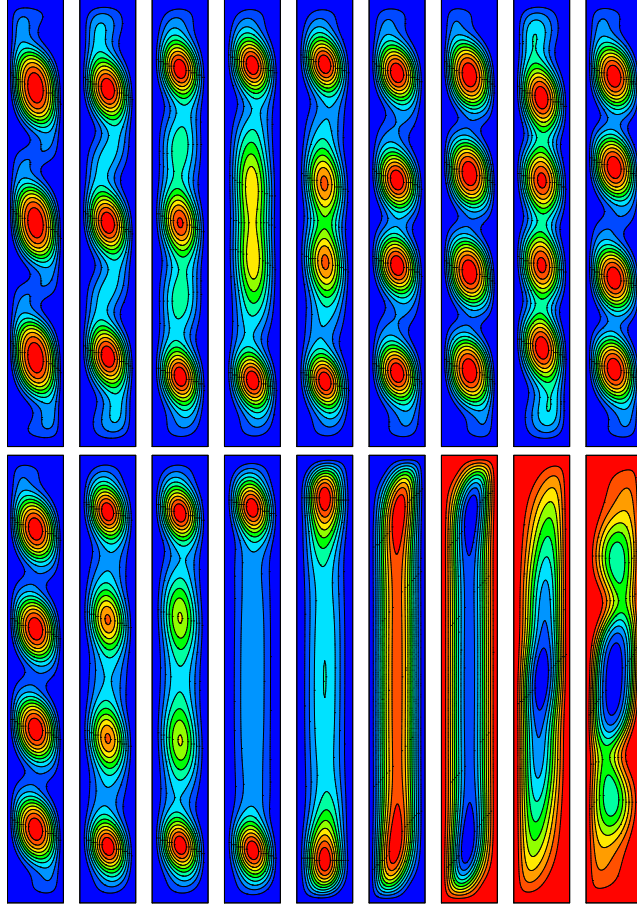
FIG. 7. From left to right and from top to bottom, sequence of contour plots of the streamfunction of the steady solutions following the primary branch of Fig. 6(a), starting from the left. The first and last plots, corresponding to $Ra^T = 1000$ and $30000$ are out of the window of parameters shown in that figure. Both solutions are stable. The location of the rest is marked with a cross on the detailed figures at 10000, 11844 (both stable), 11804, 11822, 10000, 5273.3, 10100, 7587.4, 6924.2, 12207 (the last two stable), 12167, 12533 (stable), 12653, 12895, 12900 and 15076 (the last three stable).

are located at $Ra^T = 12651$ and $Ra^T = 12662$.

Figure 9 shows a sample of the steady states of broken symmetry found at the pitchfork bifurcations. The locations of the selected points are signaled on the details of Fig. 6 in red color on the red secondary branches. In this case the fluid mainly forms four vortices of different intensity and distance between them because most of the pitchfork bifurcations are placed in segments where the primary branch has four vortices. The last two plots, which belong to stable solutions, (see Figs 7(f) and (g)) are set on a segment connecting

20
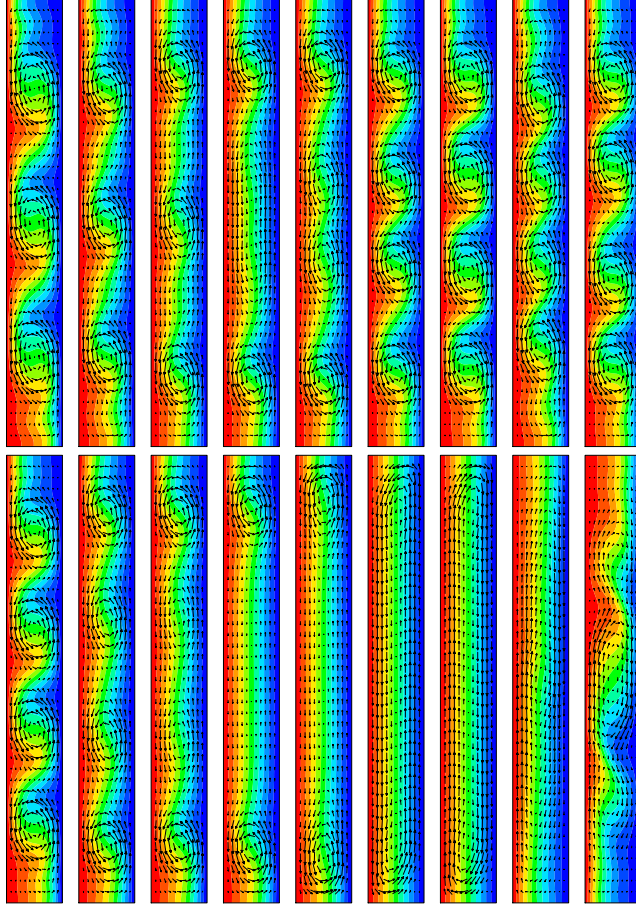
FIG. 8. Idem Fig. 7 for the concentration, and superposed velocity field (arrows).

two turning points of the secondary branches. Notice that the last corresponds to a branch starting in a point where the primary flow has just two small vortices at top and bottom, therefore when the flow becomes asymmetric one of the two vortices weakens, and can even disappear.

Figure 10 shows the superposition of the contour plots of the concentration and the velocity field at the same points as those of the streamfunction. As before, the velocity field determines the shape of the concentration and temperature profiles, asymmetric in these cases.

## C. Dynamics far from the BBC

The fluid starts oscillating at lower $Ra^T$ than for the preceding case when $Ra^C$ is increased, and the oscillations are stable for increasingly larger intervals of $Ra^T$. Figure 11(a) shows
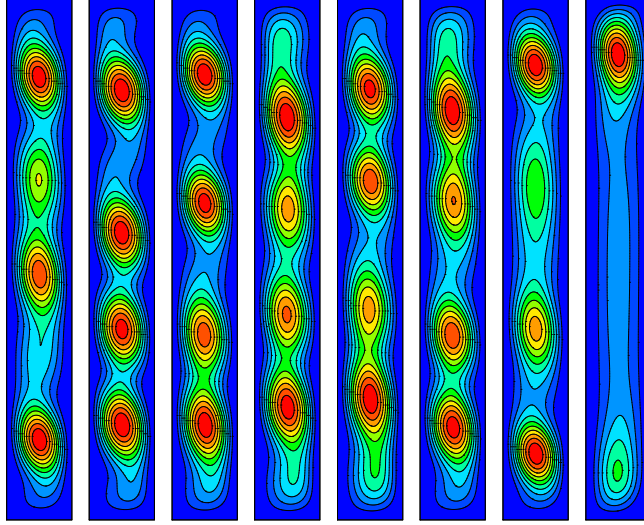
FIG. 9. Contour plots of the streamfunction of steady solutions with broken symmetry on the secondary branches of Fig. 6. Their locations are marked with a red cross in the details of the figure at $Ra^T = 11824$ (P1-P2), 10714 (P3-P6), 11705 (P3-P6), 11208 (P4-P5), 11458 (P4-P5), 11537 (P4-P5), 12188, (P7-P8) 12655 (P9-P10). The last two belong to stable solutions.
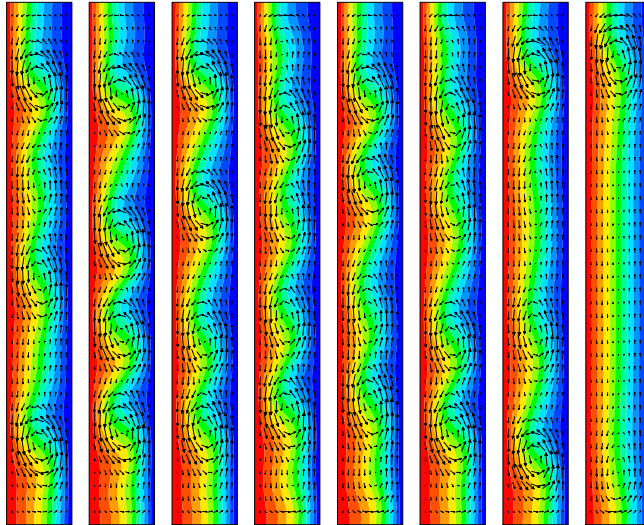


FIG. 10. Idem Fig. 9 for the concentration, and superposed velocity field (arrows).

the bifurcation diagram of the SS (in black) and PO (in red) for $Ra^C = 2250$, 3000 and 4000. At 2250 the fluid undergoes a first supercritical HB at $Ra^T = 2595.1$, which maintains the center symmetry of the flow, and a second subcritical HB at $Ra^T = 4984.2$ when the unstable pair of eigenvalues crosses back the imaginary axis. Consequently, the steady flow regains stability. A stable periodic orbit emerges from the first point that reconnects with the steady
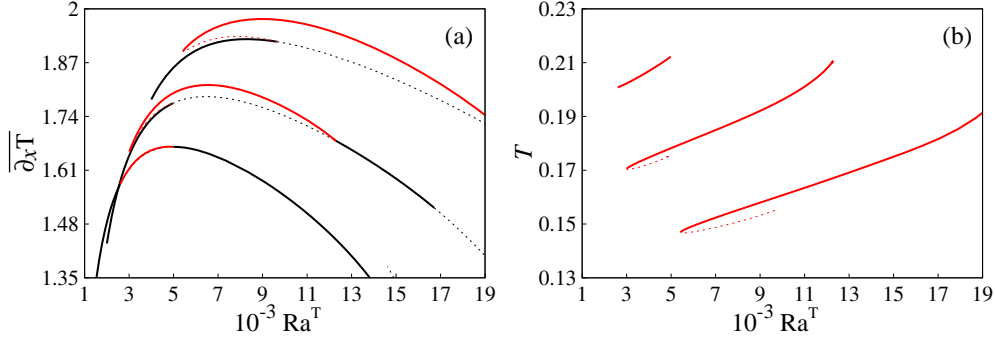
FIG. 11. (a) Idem Fig. 1 for $\mathrm{Ra}^C = 2250$, 3000 and 4000, from bottom to top. (b) The correspond-ing period of the oscillations, from top to bottom.

branch at the second critical point. The Nusselt number of the oscillations is almost that of the steady flow, as can be seen in the figure. The same holds for $\overline{K}$. At $\mathrm{Ra}^T = 14033$ there is a third HB out of the region shown that destabilizes the steady branch.

The bifurcation diagram for the onset of the oscillations for the other $\mathrm{Ra}^C$ considered is similar to that of $\mathrm{Ra}^C = 2250$, however the first HB is subcritical and takes place at $\mathrm{Ra}^T = 4955.8$ for $\mathrm{Ra}^C = 3000$, so the periodic flow is initially unstable. The critical eigenfunction also maintains the center symmetry. They become stable at $\mathrm{Ra}^T = 3004.8$ in a turning point, giving rise to the coexistence of stable steady and periodic flows in a wide range of $\mathrm{Ra}^T$. As before, the loop closes on the branch of SS at $\mathrm{Ra}^T = 12290$, where the steady solutions recover the stability up to $\mathrm{Ra}^T = 16719$ when a HB breaking the symmetry of the SS takes place. There is a fourth HB at $\mathrm{Ra}^T = 19923$, which gives rise to a branch of unstable periodic orbits (not continued).

The bifurcation diagram for $\mathrm{Ra}^C = 4000$ only differs of that found for $\mathrm{Ra}^C = 3000$ in the second HB that now is slightly supercritical, so the oscillations destabilize in a saddle-node bifurcation out of the range of Fig. 11. The first subcritical HB is found at $\mathrm{Ra}^T = 9653.2$, and critical eigenfunction maintains the center symmetry of the SS. The first saddle-node is located at $\mathrm{Ra}^T = 5423.8$, where the branch of PO becomes stable up to the second turning point located near $\mathrm{Ra}^T = 19926$, and the loop closes at $\mathrm{Ra}^T = 19889$, where the SS become stable again. In the three cases the steady branch has turning points at larger $\mathrm{Ra}^T$. The period of the oscillations for the three cases is shown in Fig. 11(b). High values of $\mathrm{Ra}^C$ tend to stabilize the symmetric oscillations, and to decrease their periods.

Figure 12(a) shows the bifurcation diagram for $\mathrm{Ra}^C = 4000$, including the branch of PO
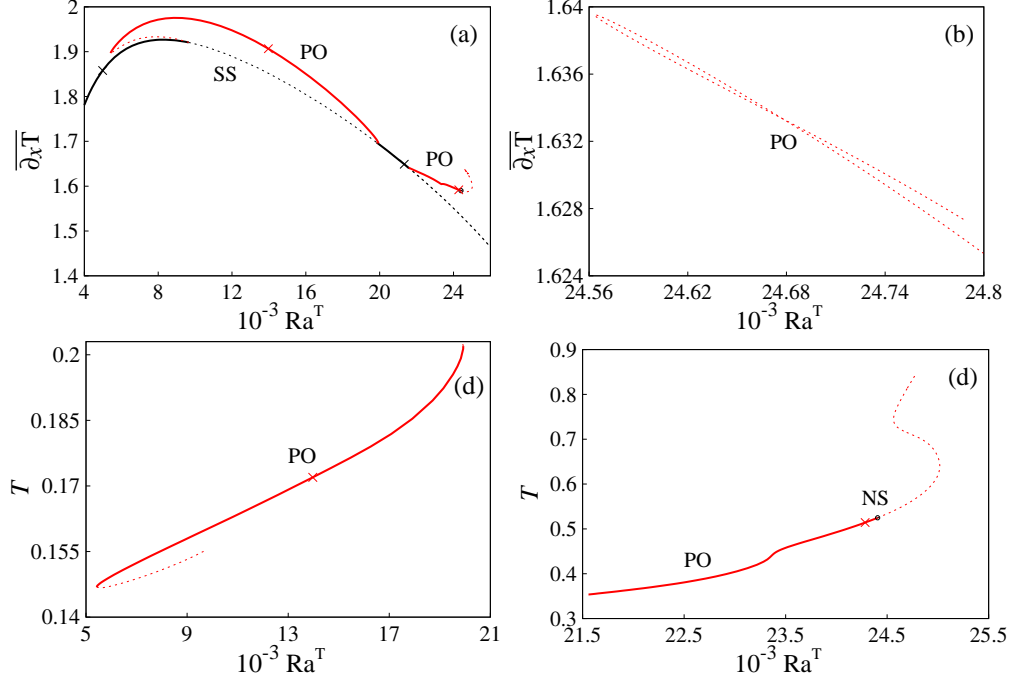
FIG. 12. (a) Idem Fig. 1 for $Ra^C = 4000$. (b) detail of (a) showing the second fold on the second branch of periodic orbits at the end of the range of parameters calculated. (c) and (d) period of the PO versus $Ra^T$.

arising at $Ra^T = 21558$ when the SS recover the stability . This bifurcation breaks the center symmetry giving rise to a branch of stable asymmetric PO, which in turn loses stability in a Neimark-Sacker (NS) bifurcation near $Ra^T = 24409$. Quasiperiodic flows emerge from this point. The comparison of the new frequency of these solutions given by the Fourier spectra of temporal evolutions, taking as initial condition the unstable PO, with that given by the critical multiplier, indicates that the bifurcation is supercritical. The similarity of the contour plots and of the amplitude of the oscillations before and after the NS also points in this direction. The unstable curve of periodic solutions shows a first fold at $Ra^T = 25019$, and a second at $Ra^T = 24563$ [see Fig. 12(b) and (d)]. At these points two real multipliers cross forward the unit circle consecutively. The branch continues being unstable up to the last PO computed, where the leading complex multiplier reaches modulus $\mathcal{O}(10^4)$, so it is unlikely that they recover the stability at larger $Ra^T$.

Figure 13 shows the contour plots of the streamfunction of a steady solution, and some equidistant snapshots in a period of a stable center-symmetric periodic orbit after the first HB. The three vortices of high intensity remain visible up to the end of the interval shown for

24
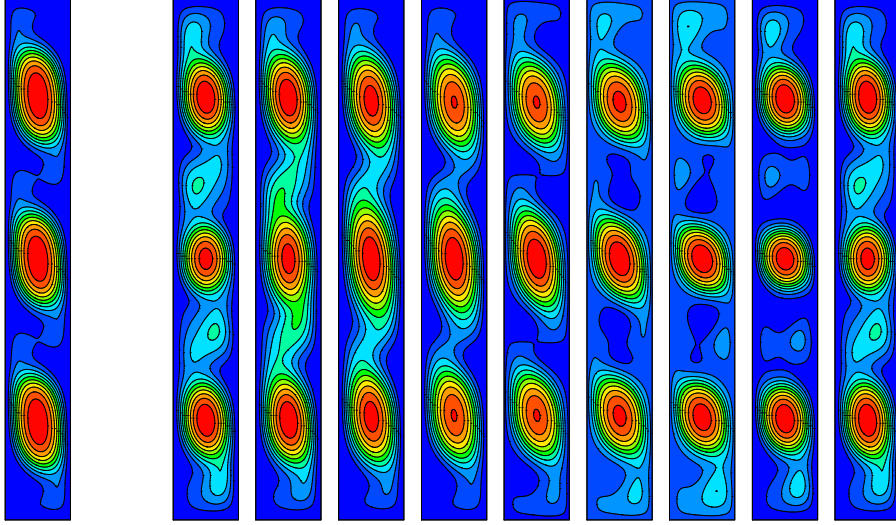
FIG. 13. Idem Fig. 2 for $Ra^T = 4991.6$ at left, and for the periodic orbit at $Ra^T = 13973$, with $T = 0.17197$ at right. $Ra^C = 4000$.

both the SS and the PO. Similar dynamics was found for $Ra^C = 2250$ and for $Ra^C = 3000$. The oscillations consist in the intensification and enlargement of the vortices, followed by the synchronous recovering of the initial size and intensity. This effect is more pronounced in the central one. In this case the vortices do not travel. At higher $Ra^T$ in the unstable part of the steady branch (not shown) new vortices appear as happens in Fig. 7 but the fluid never stabilizes.

When the symmetry is broken at $Ra^T = 21558$ (see Fig. 14) the dynamics of the oscillations consists in the appearance of a weak vortex between the upper and central vortices and below the lower during a semi-period, and between the lower and central vortices and above the upper during the second semi-period. In this way, when the central vortex goes up, the others go down and vice versa. This gives rise to a displacement of the vortices up and down that generates a vertical traveling wave that retains the following spatio-temporal symmetry

$$(\psi, \Theta, \Sigma)(t, 1 - x, \Gamma - y) = (\psi, -\Theta, -\Sigma)(t + T/2, x, y), \tag{31}$$

which means

$$(u, v)(t, 1 - x, \Gamma - y) = -(u, v)(t + T/2, x, y). \tag{32}$$

For these waves (symmetric cycles) advancing half a period in time is equivalent to applying
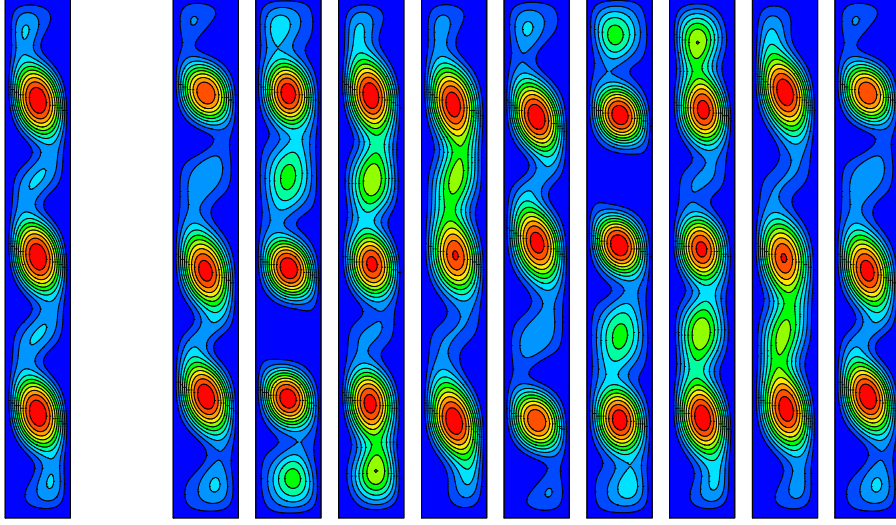
FIG. 14. Idem Fig. 2 for $\mathrm{Ra}^{\mathrm{T}} = 21335$ at left, and for the periodic orbit at $\mathrm{Ra}^{\mathrm{T}} = 24284$, with $T = 0.51413$ at right. $\mathrm{Ra}^{\mathrm{C}} = 4000$.

$\mathcal{S}$. This property allows to halve the computational cost of the time integration during the continuation process, and the time needed to obtain these type of branches.

## IV. DISCUSSION

The mechanisms leading to the onset of periodic regimes from the equilibria, can be established from the kinetic energy balance for the perturbation, obtained from the momentum equation. The details for a pure fluid and a binary mixture contained into impermeable sides can be found in Refs. [12, 36]. The growth rate of the eigenvalue at the HB points is zero, then the spatial average of the kinetic energy equation for the perturbation, with non-slip boundary conditions, is just a balance between the rate of kinetic energy generated by the shear of the steady field,

$$\overline{K}_{sh} = \Re\left( - \int_{\Omega} v_i'^* v_j' \frac{\partial v_i}{\partial x_j} \, d\Omega \right),$$ (33)

by the work done by the thermal buoyancy per unit time,

$$\overline{K}_{bT} = \Re\left( \mathrm{Ra}^{\mathrm{T}} \Pr \int_{\Omega} v_i'^* T' \delta_{i2} \, d\Omega \right),$$ (34)

by that done by the solutal buoyancy per unit time,

$$\overline{K}_{bC} = \Re\left( -\mathrm{Ra}^{\mathrm{C}} \mathrm{Le} \int_{\Omega} v_i'^* C' \delta_{i2} \, d\Omega \right),$$ (35)

26

TABLE IV. Rate of the kinetic energy generated at the transition from SS to PO by the shear, $\overline{K}_{sh}$, by the buoyancy forces, $\overline{K}_{bT}$ and $\overline{K}_{bC}$, and dissipated, $\overline{K}_{ds}$, by the perturbations at the bifurcation points. At the transition the four terms are in balance. The rest of parameters are $\mathrm{Pr} = 0.168$, $\mathrm{Se} = 0.232$, $\mathrm{Le} = 1.238$ and $Q = 0.357$.

| $\mathrm{Ra^C}$ | $10^{-3}\,N$ | $\overline{K}_{sh}$ | $\overline{K}_{bT}$ | $\overline{K}_{bC}$ | $\overline{K}_{ds}$ |
|---|---|---|---|---|---|
| 1.0 | $2.8587\times10^3$ | 0.035647 | 0.0021495 | -0.040859 | -0.037755 |
| 1750 | 22.3813 | 1.23602 | -0.040280 | -0.10159 | -1.09417 |
| 2250 | 1.15338 | 0.55983 | -0.032886 | 0.20697 | -0.73392 |
| 2250 | 2.21518 | 0.52407 | -0.068972 | 0.22935 | -0.68443 |
| 2250 | 6.23665 | 0.61113 | 0.086869 | -0.018808 | -0.67920 |
| 3000 | 1.65194 | 0.65447 | -0.054785 | 0.23967 | -0.83938 |
| 3000 | 4.09664 | 0.53887 | -0.17725 | 0.32218 | -0.68380 |
| 3000 | 5.57284 | 0.75114 | 0.051175 | -0.020046 | -0.78227 |
| 4000 | 2.41331 | 0.77173 | -0.091016 | 0.27764 | -0.95840 |
| 4000 | 4.97227 | 0.59529 | -0.25290 | 0.39484 | -0.73708 |
| 4000 | 5.38950 | 0.86585 | 0.055282 | -0.030462 | -0.89067 |

and the rate of energy dissipated by viscosity,

$$\overline{K}_{ds} = \Re\left(-2\mathrm{Pr}\int_\Omega e'^*_{ij} e'_{ij}\, d\Omega\right), \tag{36}$$

because the rate of change of the total kinetic energy

$$\overline{K} = \left(\int_\Omega \frac{1}{2} v'^*_i v'_i d\Omega\right), \tag{37}$$

of the perturbation is zero. In Eqs. (33)-(35) $v_i$ are the components of the velocity of the steady field at the bifurcation points, $v'_i$ those of the critical eigenfunction, T' and C' the temperature and concentration of the perturbation, and * means complex conjugation. In Eq. (36), $e'_{ij}$ means the strain rate tensor of the perturbation. The contribution of these terms to the transitions of the steady flow, and the change of this balance for the different $N$ studied is given in Table IV. It shows that for the mixture studied the shear stresses are the main contributors to the instability of the steady flow, and that both buoyancies can

27

contribute to stabilize or destabilize the fluid depending on the type of bifurcation and the ratio of Rayleigh numbers. It seems that the thermal buoyancy does not contribute to the beginning of the oscillations, but it helps to dissipate the kinetic energy of the velocity field when the steady flows regain stability at large $\mathrm{Ra}^\mathrm{T}$ for large enough $\mathrm{Ra}^\mathrm{C}$ (compare $\overline{K}_{bT}$ of the first row with the seventh and tenth in the table).

As said in the introduction, the stability analysis of the steady flow of binary mixtures in vertical channels showed that, in general, it can become unstable to thermal, solutal, or hydrodynamic wave perturbations. However, in the case of gaseous mixtures with positive or slightly negative Se only the last type of waves destabilize the fluid, and for Se $\lesssim -0.5$ the instability is mainly due to the other two types [9]. This result is in agreement with the above calculations, and also in agreement with other numerical analyses [12]. On the other hand, the absence of thermal instability [10] in the range of Se and Pr studied here and in [12] (although Le is much higher) might also be connected with the large amount $\overline{K}_{sh}$ stored in these mixtures.

By adding the Dufour coupling to the energy equation the off-diagonal term $\frac{\mathrm{Le}^2 \mathrm{Q}\,\mathrm{Se}}{\mathrm{NPr}}\Delta\Sigma$ is included. The sign of this term depends on the signs of Se and $N$. Both of them are positive here, so it behaves as a positive forcing, which increases when the Rayleigh ratio decreases if the rest of parameters remain frozen. As a consequence of this increase the secondary time periodic branch of solutions becomes subcritical. Moreover, although there is a lack of systematic studies on the stability of the periodic orbits bifurcated from the steady states either with or without Soret and/or Dufour effects, it seems that the influence of the latter affects the stability of the periodic waves of the gaseous mixtures, since (as far as we know) the transition from periodic oscillations to steady solutions [see Fig. 11(a)], and the cascade of period-doubling bifurcations found here was not found in other numerical studies with other configurations [2, 3, 12]. However, steady overturning convection was already observed in several experiments, for instance in annular containers [37].

Ghorayeb and Mojtabi studied thermosolutal convection (without cross couplings) in a rectangular cavity of $\Gamma = 7$ in the BBC [1]. They found four types of localized steady states, two of them with central symmetry, while the other two where asymmetric. The origin of the symmetric states was explained in Ref. [4] within the framework of the snaking theory. According to their work, the center-symmetric localized states arise from secondary transcritical bifurcations of the primary branches (spatially periodic states) or at the saddle-

node bifurcations where the primary branches turn to larger values of the parameter.

The calculations presented for $Ra^C = 1750$ help to understand the origin of the localized asymmetric solutions with just one vortex near the top of the cavity and those asymmetric with two vortices [1]. This is because this case crosses the buoyancy balanced hyperplane transversely, so around this point some of the snaking characteristics still remain (see Fig. 6 around $Ra^T = 1.28 \times 10^3$). The asymmetric states come from pitchfork bifurcations of the steady primary flow in the snaking part of the branch near the saddle-node bifurcations. The type of asymmetry depends on the structure of the flow at the bifurcation point. Notice that this hyperplane separates the zones of clockwise and counterclockwise rotation. Smallest perturbations of the BBC are expected to keep the full snaking region [4, 5].

## V.  CONCLUSIONS

The dynamics caused by lateral thermal and solutal gradients, including the Soret and Dufour effects in a $He_2$-Xe mixture has been analyzed. It was found that it is very different depending on the relation between $Ra^T$ and $Ra^C$, when the rest of the parameters are fixed. There is a variety of stable extended and localized steady states that was not found in the absence of the externally applied solutal gradients [12]. Symmetric flows with one, two, three or four vortices, and asymmetric solution with two or four vortices were found near the BBC point. However, far from it the center-symmetric oscillations replace the steady states at low $Ra^T$, although the latter restabilize at higher $Ra^T$.

The onset of the stable oscillatory dynamics, via HBs or after saddle-nodes of PO, is located at $Ra^T = 2858.7$, 39167, 2595.1, 3004.8 and 5423.8 for $Ra^C = 1.0$, 1750, 2250, 3000 and 4000, respectively, so large solutal gradients strengthen the steady dynamics and delay the beginning of the oscillations. They appear at a $Ra^T$ about one order of magnitude greater than for fluids near the BBC scenario. The interval of stable steady primary flows after the second HB becomes smaller when $Ra^C$ is increased (see Figs. 11 and 12), then by slightly increasing this parameter a leading double-Hopf bifurcation on the branch of steady states could be determined. The dynamics around this point could differ drastically from that found here, including the local onset of temporal chaos.

The oscillations give rise to center-symmetric vertical waves for negligible solutal gradients, and the transition to complex temporal dynamics takes place through a Feigenbaum

cascade, while for larger solutal gradients the symmetric oscillations generate standing waves, and quasiperiodic flows leading to temporal chaos were found bifurcating from the asymmetric waves that arise at larger $\mathrm{Ra}^\mathrm{T}$.

The study of the BBC in gases including the Soret coupling is ongoing.

## Appendix: Variational equations

When $\mathrm{p} = \mathrm{Ra}^\mathrm{C}$ is used, the variational equations for $(\psi_1, \Theta_1, \Sigma_1)$ and $\delta\mathrm{Ra}^\mathrm{C}$ are

$$\partial_t \Delta\psi_1 + J(\Delta\psi_1, \psi) + J(\Delta\psi, \psi_1) = \mathrm{Pr}\Delta^2\psi_1 - \mathrm{Ra}^\mathrm{T}\mathrm{Pr}\,\partial_x\Theta_1 + \mathrm{Ra}^\mathrm{C}\mathrm{Le}\,\partial_x\Sigma_1 -$$
$$- \delta\mathrm{Ra}^\mathrm{C}\mathrm{Le}(1 - \partial_x\Sigma) \tag{A.1}$$

$$\partial_t \Theta_1 + J(\Theta_1, \psi) + J(\Theta, \psi_1) = (1 + \mathrm{Le}\,\mathrm{Q}\,\mathrm{Se}^2)\Delta\Theta_1 + \frac{\mathrm{Le}^2\mathrm{Q}\,\mathrm{Se}}{\mathrm{NPr}}\Delta\Sigma_1 +$$
$$+ \delta\mathrm{Ra}^\mathrm{C}\frac{\mathrm{Le}^2\mathrm{Q}\,\mathrm{Se}}{\mathrm{Ra}^\mathrm{T}\mathrm{Pr}}\Delta\Sigma + \partial_y\psi_1, \tag{A.2}$$

$$\partial_t \Sigma_1 + J(\Sigma_1, \psi) + J(\Sigma, \psi_1) = \mathrm{Le}\Delta\Sigma_1 + \mathrm{N}\,\mathrm{Pr}\,\mathrm{Se}\Delta\Theta_1 - \delta\mathrm{Ra}^\mathrm{C}\frac{\mathrm{Pr}\,\mathrm{Se}\,\mathrm{N}}{\mathrm{Ra}^\mathrm{C}}\Delta\Theta + \partial_y\psi_1. \tag{A.3}$$

When $\mathrm{p} = \mathrm{Pr}$ is used, the equations for $(\psi_1, \Theta_1, \Sigma_1)$ and $\delta\mathrm{Pr}$ are

$$\partial_t \Delta\psi_1 + J(\Delta\psi_1, \psi) + J(\Delta\psi, \psi_1) = \mathrm{Pr}\Delta^2\psi_1 - \mathrm{Ra}^\mathrm{T}\mathrm{Pr}\,\partial_x\Theta_1 + \mathrm{Ra}^\mathrm{C}\mathrm{Le}\,\partial_x\Sigma_1 +$$
$$+ \delta\mathrm{Pr}\,\mathrm{Ra}^\mathrm{T}(1 - \partial_x\Theta) + \delta\mathrm{Pr}\,\Delta^2\psi \tag{A.4}$$

$$\partial_t \Theta_1 + J(\Theta_1, \psi) + J(\Theta, \psi_1) = (1 + \mathrm{Le}\,\mathrm{Q}\,\mathrm{Se}^2)\Delta\Theta_1 + \frac{\mathrm{Le}^2\mathrm{Q}\,\mathrm{Se}}{\mathrm{NPr}}\Delta\Sigma_1 -$$
$$- \delta\mathrm{Pr}\frac{\mathrm{Le}^2\mathrm{Q}\,\mathrm{Se}}{\mathrm{NPr}^2}\Delta\Sigma + \partial_y\psi_1, \tag{A.5}$$

$$\partial_t \Sigma_1 + J(\Sigma_1, \psi) + J(\Sigma, \psi_1) = \mathrm{Le}\Delta\Sigma_1 + \mathrm{N}\,\mathrm{Pr}\,\mathrm{Se}\Delta\Theta_1 + \delta\mathrm{Pr}\,\mathrm{N}\,\mathrm{Se}\Delta\Theta + \partial_y\psi_1. \tag{A.6}$$

When $\mathrm{p} = \mathrm{Le}$ is used, the equations for $(\psi_1, \Theta_1, \Sigma_1)$ and $\delta\mathrm{Le}$ are

$$\partial_t \Delta\psi_1 + J(\Delta\psi_1, \psi) + J(\Delta\psi, \psi_1) = \mathrm{Pr}\Delta^2\psi_1 - \mathrm{Ra}^\mathrm{T}\mathrm{Pr}\,\partial_x\Theta_1 + \mathrm{Ra}^\mathrm{C}\mathrm{Le}\,\partial_x\Sigma_1 -$$
$$- \delta\mathrm{Le}\,\mathrm{Ra}^\mathrm{C}(1 - \partial_x\Sigma) \tag{A.7}$$

$$\partial_t \Theta_1 + J(\Theta_1, \psi) + J(\Theta, \psi_1) = (1 + \mathrm{Le}\,\mathrm{Q}\,\mathrm{Se}^2)\Delta\Theta_1 + \frac{\mathrm{Le}^2\mathrm{Q}\,\mathrm{Se}}{\mathrm{NPr}}\Delta\Sigma_1 +$$
$$+ \delta\mathrm{Le}\,\mathrm{Q}\,\mathrm{Se}^2\Delta\Theta + \delta\mathrm{Le}\frac{2\mathrm{Le}\,\mathrm{Q}\,\mathrm{Se}}{\mathrm{NPr}}\Delta\Sigma + \partial_y\psi_1, \tag{A.8}$$

$$\partial_t \Sigma_1 + J(\Sigma_1, \psi) + J(\Sigma, \psi_1) = \mathrm{Le}\Delta\Sigma_1 + \mathrm{N}\,\mathrm{Pr}\,\mathrm{Se}\Delta\Theta_1 + \delta\mathrm{Le}\Delta\Sigma + \partial_y\psi_1. \tag{A.9}$$

The above variational systems with their boundary conditions maintain the center symmetry of Eqs. (13)-(15) together with conditions (16), (11) and (12).

[1] K. Ghorayeb and A. Mojtabi, "Double diffusive convection in a vertical rectangular cavity," Physics of Fluids **9**, 2339–2348 (1997).

[2] S. Xin, P. Le Quéré, and L. Tuckerman, "Bifurcation analysis of doubly-diffusive convection with opposing horizontal thermal and solutal gradients," Phys. Fluids **10**, 850–858 (1998).

[3] M. Mamou, "Stability analysis of thermosolutal convection in a vertical packed porous enclosure," Phys. Fluids **14**, 4302–4314 (2002).

[4] A. Bergeon and E. Knobloch, "Periodic and localized states in natural doubly diffusive convection," Physica D **237**, 1139–1150 (2008).

[5] A. Bergeon and E. Knobloch, "Spatially localized states in natural doubly diffusive convection," Phys. Fluids **20**, 034102–1–034102–8 (2008).

[6] C. Beaume, A. Bergeon, and E. Knobloch, "Convectons and secondary snaking in three-dimensional natural doubly diffusive convection," Phys. Fluids **25**, 024105–1–024105–15 (2013).

[7] S. Legare, A. Grace, and M. Stastna, "Double-diffusive instability in a thin vertical channel," Physics of Fluids **33**, 114106 (2021).

[8] G. Z. Gershuni, E. M. Zhukhovitskii, and L. E. Sorokin, "On stability of a plane-parallel convective flow of a binary mixture," J. Appl. Math. Mech. **44**, 582–586 (1980).

[9] G. Z. Gershuni, E. M. Zhukhovitskii, and L. E. Sorokin, "On stability of convective flow of a binary mixture with thermal diffusion," J. Appl. Math. Mech. **46**, 54–57 (1982).

[10] T. P. Lyubimova and N. I. Lobov, "Stability and stationary plane-parallel flow of binary fluid with the Soret effect in a vertical layer with differentially heated boundaries," Microgravity Sci. Tec. **31**, 709–714 (2019).

[11] G. Z. Gershuni, E. M. Zhukhovitskii, and A. A. Nepomnyashchy, *Stability of Convective Flows* (Nauka, 1989).

[12] J. Sánchez and M. Net, "Stationary flows and periodic dynamics of binary mixtures in tall laterally heated slots," in *Computational Modelling of Bifurcations and Instabilities in Fluid Mechanics. Computational Methods in Applied Sciences*, edited by Alexander Gelfgat (Springer, 2018) pp. 171–216.

[13] J. Liu and G. Ahlers, "Rayleigh-Bénard convection in binary-gas mixtures: Thermophysical properties and the onset of convection," Phys. Rev. E **55**, 6950–6968 (1997).

[14] S. J. Linz, "Binary mixtures: Onset of Dufour driven convection," Phys. Rev. A **40**, 7175–7181 (1989).

[15] W. Hort, S. J. Linz, and M. Lücke, "Onset of convection in binary gas mixtures: Role of the Dufour effect," Phys. Rev. A **45**, 3737–3747 (1992).

[16] St. Hollinger and M. Lücke, "Influence of the Soret effect on convection of binary fluids," Phys. Rev. E **57**, 4238–4249 (1998).

[17] St. Hollinger and M. Lücke, "Influence of the Dufour effect on convection in binary gas mixtures," Phys. Rev. E **52**, 642–657 (1995).

[18] W. Barten, M. Lücke, M. Kamps, and R. Schmitz, "Convection in binary fluid mixtures. II Localized travelling waves," Phys. Rev. E **51**, 5662–5680 (1995).

[19] O. Batiste, E. Knobloch, I. Mercader, and M. Net, "Simulations of oscillatory binary fluid convection in large aspect ratio containers," Phys. Rev. E **65**, 016303(1–19) (2001).

[20] P. Kolodner, "Repeated transients of weakly nonlinear traveling-wave convection," Phys. Rev. E **47**, 1038–1048 (1993).

[21] I. Filahi, M. Bourich, M. Hasnaoui, and A. Amahmid, "Analytical and numerical study of Soret and Dufour effects on thermosolutal convection in a horizontal Brinkman porous layer with a stress-free upper boundary," Math. Probl. Eng. **2020**, 4046570 (2020).

[22] A. F. Al-Mudhaf, A. M. Rashad, S. E. Ahmed, A. J. Chamkha, and S. M. M. El-Kabeir, "Soret and Dufour effects on unsteady double diffusive natural convection in porous trapezoidal enclosures," Int. J. Mech. Sci. **140**, 172–178 (2018).

[23] Z.-C. Hu and X.-R. Zhang, "Onset of convection in a near-critical binary fluid mixture driven by concentration gradient," J. Fluid Mech. **848**, 1098–1126 (2018).

[24] S. R. de Groot and P. Mazur, *Non-Equilibrium Thermodynamics* (Dover Publications, Amsterdam, 1962).

[25] J. Lee, M. T. Hyun, and K. W. Kim, "Natural convection in confined fluids with combined horizontal temperature and concentration gradients," Int. J. Heat Mass Transfer **31**, 1969–1977 (1988).

[26] H. Han and T. H. Kuehn, "Double diffusive natural convection in a vertical rectangular enclosure—I. experimental study," Int. J. Heat Mass Transfer **34**, 449–459 (1991).

[27] D. Laroze, J. Martínez-Mardones, and J. Bragard, "Thermal Convection in a Rotating Binary Viscoelastic Liquid Mixture," Eur. Phys. J. Spec. Top. **146**, 291–300 (2007).

[28] L. Yacine, A. Mojtabi, R. Bennacer, and A. Khouzam, "Soret-driven convection and separation of binary mixtures in a horizontal porous cavity submitted to cross heat fluxes," Int. J. Therm. Sci. **104**, 29–38 (2016).

[29] M. S. Thurlow, B. J. Brooks, P. G. J. Lucas, M. R. Ardron, J. K. Bhattacharjee, and A. L. Woodcraft, "Convective instability in rotating liquid 3He-4He mixtures," J. Fluid Mech. **313**, 381–407 (1996).

[30] M. Pozzo, C. Davies, D. Gubbins, and D. Alfè, "Transport properties for liquid silicon-oxygen-iron mixtures at Earth's core conditions." Phys. Rev. B **87**, 014110–1–014110–10 (2013).

[31] R. Peyret, *Spectral methods for incompressible viscous flow*, Applied Mathematical Sciences, Vol. 148 (Springer, 2002).

[32] J. Sánchez, M. Net, B. García-Archilla, and C. Simó, "Newton-Krylov continuation of periodic orbits for Navier-Stokes flows," J. Comput. Phys. **201**, 13–33 (2004).

[33] M. Net and J. Sánchez, "Continuation of bifurcations of periodic orbits for large-scale systems," SIAM J. Appl. Dyn. Syst. **14**, 674–698 (2015).

[34] J. Sánchez and M. Net, "Numerical continuation methods for large-scale dissipative dynamical systems," Eur. Phys. J. Spec. Top. **225**, 2465–2486 (2016).

[35] M. Mamou, P. Vasseur, and M. Hasnaoui, "On numerical stability analysis of doble-diffusive convection in confined enclosures," J. Fluid Mech. **433**, 209–250 (2001).

[36] D. Henry and H. Ben Hadid, "Multiple flow transitions in a box heated from the side in low-Prandtl-number fluids," Phys. Rev. E **76**, 016314 (2007).

[37] D. R. Ohlsen, S. Y. Yamamoto, C. M. Surko, and P. Kolodner, "Transition from Traveling-Wave to Stationary Convection in Fluid Mixtures," Phys. Rev. Lett. **65**, 1431–1434 (1990).